Available online at www.sciencedirect.com
ScienceDirect
Geochimica et Cosmochimica Acta 73 (2009) 2089–2102
Geochimica et Cosmochimica Acta
www.elsevier.com/locate/gca

A model for C–O–H fluid in the Earth's mantle

Chi Zhang [a], Zhenhao Duan [b,*]

[a] School of Earth Sciences and Resources, China University of Geosciences, Beijing 100083, China
[b] Key Laboratory of the Earth's Deep Interior, Institute of Geology and Geophysics, Chinese Academy of Sciences, P.O. Box 9825, Beijing 100029, China

Received 26 August 2008; accepted in revised form 26 January 2009; available online 4 February 2009

Abstract

A model is presented for predicting the composition (H_2O, CO_2, CH_4, H_2, CO, O_2 and C_2H_6) in the C–O–H fluid system under high temperatures and pressures found in the Earth's mantle. The model is based on a molecular dynamic equation of state, statistical mechanics calculations and non-stoichiometric global free-energy minimization. Although the model is not fitted to experimental data on C–O–H speciation, it does accurately reproduce these datasets and should extrapolate at least to the depths of ~80–220 km. The model results suggest that (1) in the upper cratonic mantle, H_2O is the dominant fluid species in the C–O–H fluid system; (2) the abundance of CO_2 increases with decreasing depth, the trend of CH_4 is just the opposite; (3) the boundary between lithosphere and asthenosphere generally divides fluid systems into H_2O–CH_4+ minor species and H_2O–CO_2+ minor species, respectively; (4) it is entirely possible to generate methane and ethane and possibly other hydrocarbons under mantle conditions, confirming previously experimental results.

1. INTRODUCTION

The "carbon cycle" constitutes one of the most important areas of the earth-system-science research in this century, linking organic–inorganic, deep–shallow and energy–environmental problems. For example, what is the distribution and origin of carbon in Earth's deep interior? Do the lower crust and mantle possess abiotic carbon molecules? Many of the fundamental questions are best approached by thermodynamic modeling.

Most carbon bearing geological fluids in the Earth's crust and mantle can be ascribed to the C–O–H system, which encompasses compositions such as H_2O, CO_2, CH_4, H_2, CO, O_2, C_2H_6 and their mixtures. These fluids play significant roles in most geologic processes like fluid–rock interactions (McCollom and Shock, 1998; Zheng et al., 1999), dehydration of subducted slabs (Gerya and Yuen, 2003; Spandler et al., 2003; Rupke et al., 2004), destruction of craton (Liu, 2005), metasomatism (Stalder et al., 1998), mantle melting (Bruce Watson and Brenan, 1987; Taylor and Green, 1988), devolatilization reactions in graphitic rocks (Connolly and Cesare, 1993; Connolly, 1995) and magma degassing (Wallace et al., 2003). Fluid compositions in different geologic settings vary substantially. Thus, fluid composition is the first problem that should be solved when we try to understand the fluid origin, evolution and rock–fluid interaction involved in these processes. However, due to the difficulty in measuring the fluid speciation in the Earth's deep interior in situ, our knowledge about the composition of the C–O–H system is still limited.

Thermodynamic models offer an efficient means of predicting fluid speciation at *P*–*T* conditions met in the Earth's deep interior. Many attempts (French, 1966; Ohmoto and Kerrick, 1977; Johnson et al., 1992; Shi and Saxena, 1992; Connolly and Cesare, 1993; Larsen, 1993; Connolly, 1995; Huizenga, 2001; Kress et al., 2004; Huizenga, 2005) have been made to model fluid compositions in this system. Most models adopt the equilibrium constant-mass balance technique following the procedure proposed by French (1966), which was developed to solve the problem about homogeneous fluid phase coexisting with oversaturated solid car-

* Corresponding author.
E-mail address: duanzhenhao@yahoo.com (Z. Duan).

0016-7037/$ - see front matter © 2009 Published by Elsevier Ltd.
doi:10.1016/j.gca.2009.01.021

bon. Considering that graphite/diamond are common accessory minerals in many fluid-bearing igneous and metamorphic rocks (French, 1966), the carbon oversaturation constraint is taken and the system's degree of freedom at certain T and P is reduced to only one. The choice of the variable needed to determine the composition speciation of the system can be oxygen fugacity, f_{O_2} (French, 1966; Ohmoto and Kerrick, 1977; Huizenga, 2001), CO_2/($CH_4 + CO_2$) ratio (Frezzotti et al., 1990; Huizenga and Touret, 1999), or the atomic ratio of oxygen in total oxygen and hydrogen X_O (Connolly and Cesare, 1993; Huizenga, 2001; Kress et al., 2004), where $X_O = \frac{n_O}{n_O + n_H}$, and n_O and n_H are the moles of oxygen and hydrogen atoms, respectively. For those systems where carbon is undersaturated, the carbon activity in environment is also needed. These models have been successfully used in the study of silicate melting (Botchamikov et al., 2006), graphite/diamond formation (Sokol et al., 2001, 2004), etc.

Most previous studies considered only six major species, H_2O, CO_2, CH_4, H_2, CO and O_2, and used equilibrium constants for four independent chemical reactions for the calculation procedure. This approach is not flexible and is not easily extended to higher numbers of species. The number of independent reactions increases with the number of possible species in the system, so the whole procedure is required to be rebuilt and all explicit expressions in it are required to be rewritten. Some other models (Kress et al., 2004) adopt global free-energy minimization method which does not need to specify independent reactions and can be easily extended to handle cases containing more species or phases, such as the problem of the generation of abiogenetic methane in the Earth's mantle (Scott et al., 2004).

A strong equation of state (EOS) is essential to predict the speciation of the C–O–H fluid system in the Earth's interior. An accurate EOS requires a theoretical sound formula and reliable experimental data for the purpose of calibration. However, very few experimental data exist even for pure species under temperatures higher than 1200 K and pressures greater than 1 GPa. Furthermore, extrapolation of EOS developed for lower T and P data to higher P–T conditions can lead to substantial errors. Molecular dynamics simulations had emerged as another important means for studying the behavior of fluid species under high TP conditions. Our previous simulation results (Zhang and Duan, 2005; Duan and Zhang, 2006; Zhang et al., 2007) have been shown to extend the existing experimental range up to 2573 K and 10 GPa. As part of our work to predict the speciation of the C–O–H system, we first improve the general EOS proposed by Duan et al. (1992, 1996). The improved EOS incorporates recent progress in laboratory experiments and our results from molecular dynamics simulations (Duan and Zhang, 2006; Zhang et al., 2007) and allows for more accurate calculation of thermodynamics properties.

The model also adopts some other refinements to improve accuracy. Standard chemical potentials are calculated based on statistical mechanics. Many experiments report significant amounts of C_2H_6 (Jakobsson and Oskarsson, 1990; Matveev et al., 1997; Kenney et al., 2002), thus, we added C_2H_6 to the model as a possible specie. The appearance of C_2H_6 significantly affects the compositional results and casts doubt on previous studies. The non-stoichiometric global free-energy minimization method, which can be easily expanded to include multi-species and multi-solid phases in the calculations, is adopted to calculate the equilibrium composition.

2. CHEMICAL POTENTIALS OF POSSIBLE SPECIES

2.1. Standard chemical potential for fluid species

In general, the chemical potential μ_i of each fluid species i can be expressed as

$$\mu_i = \mu_i^0(T) + RT \ln\left(\frac{f_i}{p^0}\right) \quad (1)$$

$$f_i = x_i P \hat{\phi}_i = n_i P \hat{\phi}_i / \sum_i n_i \quad (2)$$

where μ_i^0 is chemical potential in the standard state (ideal gas at standard state pressure $p^0 = 0.1$ MPa); n_i, x_i, $\hat{\phi}_i$ and f_i are the number of moles, mole fraction, fugacity coefficient and fugacity of species i, respectively.

As indicated in Eq. (1), the chemical potential is composed of two parts. The first part on the right of the equation represents the standard chemical potential at given temperature and the second part stands for the contribution of pressure.

The standard chemical potential is calculated from the statistical mechanics. The total partition function for diatomic (q_D), linear polyatomic (q_{LP}) and non-linear polyatomic (q_{NLP}) gas in canonical ensemble is given by

$$q_D = \left(\frac{2\pi mkT}{h^2}\right)^{3/2} V \frac{8\pi^2 IkT}{\sigma h^2} e^{-h\varpi c/2kT}\left(1 - e^{-h\varpi c/kT^{-1}}\right)\omega_{e1} e^{D_e/kT} \quad (3)$$

$$q_{LP} = \left(\frac{2\pi mkT}{h^2}\right)^{3/2} V \frac{8\pi^2 IkT}{\sigma h^2} \left\{\prod_{j=1}^{3n-5} \frac{e^{-hc\varpi_j/2kT}}{1 - e^{-hc\varpi_j/kT}}\right\}\omega_{e1} e^{D_e/kT} \quad (4)$$

$$q_{NLP} = \left(\frac{2\pi mkT}{h^2}\right)^{3/2} V \frac{\pi^{1/2}}{\sigma}\left(\frac{8\pi^2 kT}{h^2}\right)^{3/2} (I_A I_B I_c)^{1/2} \times \left\{\prod_{j=1}^{3n-6} \frac{e^{-hc\varpi_j/2kT}}{1 - e^{-hc\varpi_j/kT}}\right\}\omega_{e1} e^{D_e/kT} \quad (5)$$

where I is the moment of inertia; ϖ is the wave numbers of the vibration; σ is the symmetry number; ω_{e1} is the degeneracy of ground electronic state; m is the molecular mass; and V is volume.

Then the standard chemical potential can be obtained from

$$\mu^0(T) = -kT \ln(qkT/V) + kT \ln p^0 \quad (6)$$

The spectroscopic constants and parameters for diatomic and polyatomic species are listed in Tables 1 and 2, respectively.

Table 1
Spectroscopic constants of diatomic molecules.

Molecular	ω_{e1}	ϖ^* (cm^{-1})
H_2	1	4401.21
CO	1	2169.81
O_2	3	1580.19

* Data from Huber and Herzberg (Huber and Herzberg, 1979).

Table 2
Molecular constants and parameters of polyatomic molecules (number in the brackets is the degeneracy of each mode).

Molecular	Type	σ	ϖ^* (cm^{-1})					
H_2O	Non-linear	2	3657(1)	1595(1)	3756(1)			
CO_2	Linear	2	1333(1)	667(1)	2349(2)			
CH_4	Non-linear	12	2917(1)	1534(2)	3019(3)	1306(3)		
C_2H_6	Non-linear	6	2954(1)	1388(1)	995(1)	289(1)	2896(1)	1379(1)
			2969(2)	1468(2)	1190(2)	2985(2)	1469(2)	822(2)

* Data from Shimanouchi (1972).

The calculated standard chemical potentials have been compared with those from CRC handbook (Gurvich et al., 2007). The deviations are less than 0.2% in molar Gibbs free energy. Then the second part of the chemical potential is evaluated from an equation of state.

2.2. EOS for fluid phase

The major uncertainty in modeling C–O–H fluids at elevated T and P comes from the EOS, which is used for the calculation of fugacity coefficient with the following formula:

$$\ln \hat{\phi}_i = -\frac{1}{RT}\int\left(\frac{RT}{P} - \bar{V}_i\right)dP \tag{7}$$

where $\bar{V}_i = \left(\frac{\partial V}{\partial n_i}\right)_{T,P,j\neq i}$ represents the partial molar volume. The commonly used EOSs include modified Redlich–Kwong (MRK) EOS (Holloway, 1977, 1981), Compensated-Redlich–Kwong (CORK) EOS (Holland and Powell, 1991, 1998), KJ EOS (Jacobs and Kerrick, 1981; Kerrick and Jacobs, 1981), corresponding state equations in SF EOS (Saxena and Fei, 1987), BS EOS (Belonoshko and Saxena, 1992), SS EOS (Shi and Saxena, 1992) and more recently CG EOS (Churakov and Gottschalk, 2003a,b). The predictability of these EOSs is often restricted by the theoretical simplification of interactions between fluid molecules. Most of these equations are based on data collected below (or well below) 1 GPa. Some EOS (e.g., Belonoshko and Saxena, 1992) used shockwave data to cover higher ranged of T and P. However, in shockwave data the temperature is calculated from Hugoniot relations rather than being directly measured. Thus, a PVT point in shockwave experimental data is model dependant. And EOSs based on the shockwave data can produce large deviation even within the T–P range of the experimental data. The other problem is that many of these EOSs accommodate only some of all the possible species in the C–O–H system. For instance, the EOSs of Duan and Zhang (2006) and Zhang et al. (2007) are believed to be reliable up to 10 GPa, these EOSs were developed for binary systems and they are not sufficient for modeling all the species in the C–O–H system.

For full speciation of the C–O–H system, we need a general EOS which counts all possible species. In this study, we notice that the form of general EOS proposed by Duan et al. (1992, 1996) is appropriate for the model of C–O–H fluid system. Though the basic form of this EOS was built from data of methane, it is flexible to cover all other polar and nonpolar species and their mixtures considered in our model. Thus we adopt the form of this EOS with some modifications and improve the parameters by fitting them to all possible experimental data as well as data from molecular dynamics (MD) simulations (Zhang and Duan, 2005; Duan and Zhang, 2006; Zhang et al., 2007). The enhanced EOS takes the form

$$\begin{aligned} Z = \frac{P_m V_m}{RT_m} = 1 &+ \frac{a_1 + a_2/T_m^2 + a_3/T_m^3}{V_m} + \frac{a_4 + a_5/T_m^2 + a_6/T_m^3}{V_m^2} \\ &+ \frac{a_7 + a_8/T_m^2 + a_9/T_m^3}{V_m^4} + \frac{a_{10} + a_{11}/T_m^2 + a_{12}/T_m^3}{V_m^5} \\ &+ \frac{a_{13}}{T_m^3 V_m^2}\left(a_{14} + \frac{a_{15}}{V_m^2}\right)\exp\left(-\frac{a_{15}}{V_m^2}\right) \end{aligned} \tag{8}$$

$$P_m = \frac{3.0636\sigma^3 P}{\varepsilon} \tag{9}$$

$$T_m = \frac{154T}{\varepsilon} \tag{10}$$

$$V = 1000V_m\left(\frac{\sigma}{3.691}\right)^3 \tag{11}$$

where the parameters $a_1 - a_{15}$ and the Lenard–Jones potential parameters ε, σ for different species can be found in Tables 3 and 4, respectively.

Table 5 compares the calculated results of our EOS with a large number of experimental and MD simulation data in a wide TP range (673–2573 K, 0.1–10 GPa). It can be seen from the table that the EOS reproduces all the data with high accuracy for all species considered in this study.

As an example to illustrate the superiority of the EOS of this study, Table 6 compares the EOS of this study with

Table 3
The parameters for the equation of state.

a_1	2.95177298930D − 002
a_2	−6.33756452413D + 003
a_3	−2.75265428882D + 005
a_4	1.29128089283D − 003
a_5	−1.45797416153D + 002
a_6	7.65938947237D + 004
a_7	2.58661493537D − 006
a_8	0.52126532146D + 000
a_9	−1.39839523753D + 002
a_{10}	−2.36335007175D − 008
a_{11}	5.35026383543D − 003
a_{12}	−0.27110649951D + 000
a_{13}	2.50387836486D + 004
a_{14}	0.73226726041D + 000
a_{15}	1.54833359970D − 002

Table 4
Lenard–Jones parameters for different species.

Species	ε/k_B (K)	σ (10^{-10} m)
CH_4	154.0	3.691
H_2O	510.0	2.88
CO_2	235.0	3.79
H_2	31.2	2.93
CO	105.6	3.66
O_2	124.5	3.36
C_2H_6	246.1	4.35

other general EOS in reproducing the recently experimental PVT data of pure H_2O. It can see that our EOS reproduced experimental results with average deviation of 1.5% in the high TP range. In contrast, CORK EOS (Holland and Powell,1991, 1998) and SF EOS (Saxena and Fei, 1987) predict much smaller molar volumes with average deviations of 4.8% and 8.1%, respectively. According to Eq. (7), the systematic underestimation of molar volume will transfer to the calculated fugacity coefficient from integration. It should noticed that the CG EOS (Churakov and Gottschalk, 2003a,b) based on perturbation theory yields similar accuracy in volume. However, our EOS has far fewer parameters and simper form so it is more suitable to be used in iteration due to computational efficiency.

The EOS for mixtures is constructed from the end member (pure species) EOS with a mixing rule. The Lorentz–Berthelot rules is used to mix the parameters ε and σ

$$\varepsilon = \sum_{i=1}^{n}\sum_{j=1}^{n} x_i x_j k_{1,ij}\sqrt{\varepsilon_i \varepsilon_j} \tag{12}$$

$$\sigma = \sum_{i=1}^{n}\sum_{j=1}^{n} x_i x_j k_{2,ij}(\sigma_i + \sigma_j)/2 \tag{13}$$

Table 5
Experimental and simulation data used to evaluate the Equation of state.

Specie	Experimental range	Data points	Simulation range	Number	EOS average deviation in volume (%)
CH_4	273–723 K 0.1–1015.5 MPa	1941	673–2573 K 50–10,000 MPa	237	0.98
CO_2	473–1100 K 0.1-800 MPa	5810	673–2573 K 800–10,000 MPa	213	0.94
H_2O	673–1873 K 0.1–5000 MPa	8316	673–2573 K 800–10,000 MPa	213	0.80
H_2	250–423 K 2–700 MPa	111			1.43
CO	300–573.2 K 10–1020.6 MPa	273			0.4
O_2	300–1000 K 7.0–1013.2 MPa	160			0.74
C_2H_6	373–673 K 30–900 MPa	135			1.45

where i and j refer to different species in the mixture; x_i and x_j represent the mole fraction of the corresponding species; $k_{1,ij}$ and $k_{2,ij}$ are mixing parameters to describe interaction between particular molecules. Naturally, both $k_{1,ij}$ and $k_{2,ij}$ will be equal to 1 if $i = j$. In other cases, $k_{1,ij}$ and $k_{2,ij}$ can be evaluated with binary system's data or assumed to be a default value of unity as an approximation. Table 7 summarizes results calculated for CO_2–H_2O and CH_4–H_2O systems at the P–T–X conditions where experimental and simulated data are abundant. These results show that, even if the mixing parameters are set as $k_{1,ij} = k_{2,ij} = 1$, we can still predict the PVT properties to within experimental errors. Therefore, we set all other mixing parameters except for the interactions between H_2O, CO_2 and CH_4 equal to 1.

Fig. 1 compares the experimental volume of the CO_2–H_2O system with the volume calculated from the EOS of this study, the EOS of Keririck and Jacobs (1981), CG EOS of Churakov and Gottschalk (2003a,b) and the CORK EOS of Holland and Powell (1991, 1998), It can be seen that CG EOS and our general EOS of this study give similar results within the range of experimental error whereas the KJ EOS (Jacobs and Kerrick, 1981; Kerrick and Jacobs, 1981) predicts value much higher than the experiment. The predicted value of CORK EOS (Holland and Powell, 1991, 1998) is close to the experimental results in the region of lower water contents, but deviations increase with water content.

The fugacity coefficients derived from this EOS is expressed as

$$\ln\phi_i = Z - 1 - \ln Z + S_1 + 2S_2\left(1 - \frac{\sum_j k_{1,ij}x_j\sqrt{\varepsilon_i\varepsilon_j}}{\varepsilon}\right) + 6(1-Z)\left[1 - \frac{\sum_j k_{1,ij}x_j(\sigma_i+\sigma_j)/2}{\sigma}\right] \tag{14}$$

$$S_1 = \frac{a_1 + a_2/T_m^2 + a_3/T_m^3}{V_m} + \frac{a_4 + a_5/T_m^2 + a_6/T_m^3}{2V_m^2} + \frac{a_7 + a_8/T_m^2 + a_9/T_m^3}{4V_m^4} + \frac{a_{10} + a_{11}/T_m^2 + a_{12}/T_m^3}{5V_m^5} + \frac{a_{13}}{2a_{15}T_m^3}\left[a_{14} + 1 - \left(a_{14} + 1 + \frac{a_{15}}{V_m^2}\right)\exp\left(-\frac{a_{15}}{V_m^2}\right)\right] \tag{15}$$

$$S_2 = \frac{2a_2/T_m^2 + 3a_3/T_m^3}{V_m} + \frac{2a_5/T_m^2 + 3a_6/T_m^3}{2V_m^2} + \frac{2a_8/T_m^2 + 3a_9/T_m^3}{4V_m^4} + \frac{2a_{11}/T_m^2 + 3a_{12}/T_m^3}{5V_m^5} + \frac{3a_{13}}{2a_{15}T_m^3}\left[a_{14} + 1 - \left(a_{14} + 1 + \frac{a_{15}}{V_m^2}\right)\exp\left(-\frac{a_{15}}{V_m^2}\right)\right] \tag{16}$$

2.3. Chemical potential for solid phases

For phase equilibrium calculation involving C–O–H fluid in the presence of solid carbon, the explicit Gibbs free energy equation of state proposed by Fried and Howard (2000) is used to calculated standard chemical potential $\mu_c^*(T,P)$ at given temperature and pressure. They claim that

Table 6
Comparison of calculated molar volume of H_2O from different EOS with experimental data.

T (K)	P (MPa)	V_{EXP}[a]	$V_{This\ study}$[a]	Δ (%)	V_{CG}[a]	Δ (%)	V_{CORK}[a]	Δ (%)	V_{SF}[a]	Δ (%)	Ref.[b]
1203.15	950	22.56(.36)	22.20	−1.6	22.30	−1.1	21.60	−4.3	21.39	−5.2	I
1293.15	1750	19.15(.19)	19.00	−0.8	18.89	−1.3	18.15	−5.2	17.51	−8.6	
1393.15	1750	19.54(.33)	19.52	−0.1	19.47	−0.3	18.66	−4.5	17.91	−8.3	
1491.15	950	25.86(.61)	24.88	−3.8	25.34	−2.0	24.51	−5.2	23.73	−8.3	
1493.15	1750	20.49(.24)	20.04	−2.2	20.06	−2.1	19.19	−6.4	18.30	−10.7	
1593.15	1750	21.47(.29)	20.56	−4.3	20.64	−3.9	19.71	−8.2	18.67	−13.0	
1693.15	1750	21.79(.30)	21.07	−3.3	21.22	−2.6	20.24	−7.1	19.03	−12.7	
1723.15	2200	20.15(.37)	19.64	−2.5	19.66	−2.4	18.68	−7.3	17.56	−12.8	
1873.15	2500	19.61(.31)	19.41	−1.0	19.42	−1.0	18.37	−6.3	17.15	−12.5	
1273.15	1450	20.03(.26)	19.96	−0.3	19.91	−0.6	19.17	−4.3	18.58	−7.3	II
1373.15	1450	20.83(.25)	20.58	−1.2	20.61	−1.1	19.80	−5.0	19.08	−8.4	
1473.15	1450	21.6(.28)	21.19	−1.9	21.30	−1.4	20.44	−5.3	19.56	−9.4	
1573.15	1450	22.3(.33)	21.81	−2.2	22.00	−1.3	21.08	−5.5	20.03	−10.2	
1673.15	1450	23.15(.32)	22.43	−3.1	22.70	−2.0	21.73	−6.1	20.48	−11.5	
983.15	1850	16.98	17.06	0.5	16.91	−0.4	16.39	−3.5	15.96	−6.0	III
983.15	1400	18.18	18.25	0.4	18.10	−0.4	17.58	−3.3	17.17	−5.5	
983.15	2500	15.79	15.90	0.7	15.77	−0.1	15.24	−3.5	14.89	−5.7	
1173.15	3000	15.79	16.00	1.3	15.77	−0.1	15.14	−4.1	14.75	−6.6	
1173.15	3500	15.38	15.41	0.2	15.18	−1.3	14.55	−5.4	14.23	−7.5	
1273.15	3000	16.22	16.35	0.8	16.11	−0.7	15.43	−4.9	14.96	−7.8	
1273.15	2950	16.27(.18)	16.42	0.9	16.19	−0.5	15.50	−4.8	15.02	−7.7	
1273.15	2450	16.69(.13)	17.23	3.2	17.03	2.0	16.32	−2.2	15.78	−5.5	
1373.15	3000	16.51	16.68	1.1	16.46	−0.3	15.72	−4.8	15.17	−8.1	
1373.15	4000	15.25	15.48	1.5	15.22	−0.2	14.50	−4.9	14.11	−7.5	
1373.15	2500	17.31	17.53	1.3	17.35	0.2	16.58	−4.2	15.95	−7.9	
1373.15	3500	15.65	16.02	2.4	15.78	0.8	15.04	−3.9	14.58	−6.8	
1073.15	850	21.63(0.21)	21.71	0.4	21.71	0.4	21.10	−2.4	21.14	−2.3	IV
1073.15	1500	18.52(.09)	18.54	0.1	18.37	−0.8	17.78	−4.0	17.33	−6.4	
1073.15	2000	17.19(.31)	17.23	0.2	17.04	−0.9	16.46	−4.3	16.00	−6.9	
1173.15	850	23.54(.25)	22.73	−3.4	22.86	−2.9	22.18	−5.8	22.15	−5.9	
1173.15	2000	17.65(.29)	17.73	0.4	17.54	−0.7	16.89	−4.3	16.37	−7.3	
Average				1.5		1.2		4.8		8.1	

[a] The label CG, CORK and SF represent value calculated from CG EOS (Churakov and Gottschalk, 2003a,b), CORK EOS (Holland and Powell, 1991, 1998), and SF EOS (Saxena and Fei, 1987). All molar volume values here take the unit cm^3/mol.
[b] Experimental results of (I) Brodholt and Wood (1994), (II) Frost and Wood (1997b), (III) Withers et al. (2000) and (IV) Larrieu and Ayers (1997).

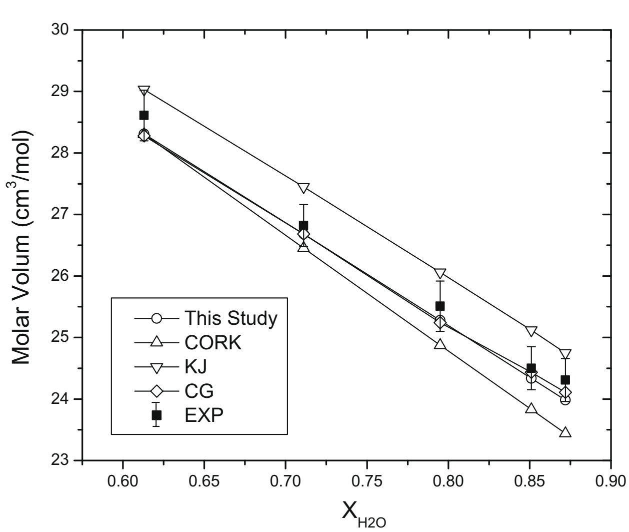

Fig. 1. Comparison of experimental molar volume (Frost and Wood, 1997b) with different equations of state in the H_2O–CO_2 system at 1573.15 K, 1.45 GPa. The label CG, CORK and KJ represent value calculated from CG EOS (Churakov and Gottschalk, 2003a,b), CORK EOS (Holland and Powell, 1991, 1998), and KJ EOS (Jacobs and Kerrick, 1981; Kerrick and Jacobs, 1981).

Table 7
The mixture parameters and average error in volume of the CO_2–H_2O and CH_4–H_2O systems.

	$k_{1,ij}$	$k_{1,ij}$	TP range	Data points	Average error in volume (%)	Average error in volume (%) ($k_1 = k_2 = 1$)
CO_2–H_2O	0.85	1.02	673–2573 K 1–10,000 MPa	1840	1.12	2.27
CH_4–H_2O	0.8	1.0	673–2573 K 10–10,000 MPa	1180	1.97	2.68

their equation produces accurate results in the range $0 \leqslant P \leqslant 600$ GPa and $300 \leqslant T \leqslant 15000$ K. The chemical potential μ_c is express as

$$\mu_c = \mu_c^*(T,P) + RT\ln a_c \tag{17}$$

where carbon activity a_c is introduced to handle carbon unsaturated condition.

3. GLOBAL FREE ENERGY MINIMIZATION ALGORITHM

The system's total free-energy G_s is a function of temperature, pressure, and the molar concentrations of each species in all phases. The problem of equilibrium speciation in the C–O–H system is formulated as one of minimization of G_s at given T and P subject to the element-abundance constraint.

$$\min G_s = \sum_{i=1}^{N_s+N_m} n_i\mu_i \tag{18}$$

$$\sum_{i=1}^{N} a_{ji}n_i = b_j \quad j = 1,2,\cdots,M \tag{19}$$

where N_m represents the number of species in the multi-species phase (e.g., seven species are considered in the homogeneous fluid phase) N_s stands for the number of species in the single species phase (e.g., the solid phase of graphite or diamond in the carbon oversaturated system); M represents the number of elements and a_{ji} is the subscript to the j element in the molecular formula of species i. The variable n_i and b_j denote the amount of species i and j element, respectively.

The Lagrange multipliers λ_j are introduced into Eq. (18), which turns the problem into one of searching for the minimum of the function ς

$$\varsigma(n,\lambda) = \sum_{i}^{N_s+N_m} n_i\mu_i + \sum_{j}^{M}\lambda_j\left(b_j - \sum_{i}^{N_s+N_m} a_{ji}n_i\right) \tag{20}$$

The necessary condition for the minimization provides $N_s + N_m + M$ equations:

$$\frac{\partial\varsigma}{\partial n_k} = \mu_k - \sum_{j}^{M} a_{jk}\lambda_j = 0 \quad k = 1,2,\cdots,N_s+N_m \tag{21}$$

$$\frac{\partial\varsigma}{\partial\lambda_j} = b_j - \sum_{i}^{N_s+N_m} a_{ji}n_i = 0 \quad j = 1,2,\cdots,M \tag{22}$$

A modified version of non-stoichiometric global free-energy minimization RAND algorithm proposed by Smith and Missen (1982) is found to be particularly robust and effective to solve the problem of equilibrium speciation in the C–O–H system. In this algorithm, Eqs. (21) and (22) are solved iteratively with the Newton–Raphson method after Eqs. (1) and (17) are substituted into for chemical potential. Then the number of equations to be solved on each iteration is $\pi_s + \pi_m + M$, where π_s and π_m are the number of single species phase and multi-species phase, respectively. These equations consist of

$$\sum_{i=1}^{M}\sum_{k=1}^{N_s+N_m} a_{ik}a_{jk}n'_k\frac{\delta\lambda_i}{RT} + \sum_{\alpha=1}^{N_s+N_m} b'_{j\alpha}u_\alpha = \sum_{k=1}^{N_s+N_m} a_{jk}n'_k\frac{\mu'_k}{RT} + b_j - b'_j \quad j = 1,2\ldots M \tag{23}$$

$$\sum_{i=1}^{M} b'_{i\alpha}\frac{\delta\lambda_i}{RT} = \sum_{k=1}^{N_s+N_m} n'_{k\alpha}\frac{\mu'_{k\alpha}}{RT} \quad \alpha = 1,2\ldots\pi_s+\pi_m \tag{24}$$

where u_α is defined by $u_\alpha = \sum_i\delta n_i/\sum_i n_i$ in α phase, and δn and $\delta\lambda$ are the steps of the numbers of moles and the Lagrange multipliers, respectively. By providing an estimate for the amount of species n', the amount of the element $b'_j = \sum_{i=1}^{N} a_{ji}n'_i$ and the chemical potential μ'_k are calculated from Eq. (1) for a given fugacity coefficient. The linear Eqs. (23) and (24) are then solved unknowns u_α and $\delta\lambda_i$. Then δn_j in the multi-species and single-species phases are calculated with following from

$$\delta n_j = n'_j\left(\sum_{i=1}^{M}\frac{a_{ij}\gamma_i}{RT} + u_\alpha - \frac{\mu'_j}{RT}\right) \tag{25}$$

$$\delta n_j = u_\alpha n'_j, \tag{26}$$

respectively.

After all δn_j are solved, the amount of such species is updated with $n'_j + \delta n'_j$ and the iteration continues until each δn_j converges to zero.

In this study, an additional loop outside the original RAND algorithm mentioned above is used to handle the nonideal behavior of mixed fluids. The fugacity coefficients in Eq. (2) are fixed during the run of RAND algorithm. Once an equilibrium speciation is found, an EOS is used to update the fugacity coefficients with calculated molar fraction. Then the RAND algorithm is called again with updated fugacity coefficients. The procedure repeats until the change of fugacity coefficients converge within given tolerance.

4. VALIDATION OF THE MODEL WITH EXPERIMENTAL DATA

The most direct method to validate a model is to compare the model prediction with as many experimental data as possible. Although the importance of the C–O–H system on the Earth and on other planets is obvious, the experimental data in the high TP range are surprisingly limited. This is because of the difficulty in performing well controlled experiments at these P–T conditions. Here we compare the model to available experimental results for CO_2 fugacity, equilibrium speciation compositions of fluids and diamond-fluid equilibrium, which were not used in the model parameterization.

4.1. Model prediction of CO_2 fugacity data

The reliability of the speciation equilibrium model depends on the accuracy of the calculation of the species fugacity, which is generally calculated from an EOS. Table 8 compares the calculated CO_2 fugacity from different EOS and the experimental phase equilibrium data for decarbonization reactions as discussed by Bottinga and Richet (1981) and Saxena and Fei (1987). The deviations in calculated fugacity from our EOS are comparable with the differences between different experimental results.

4.2. Model prediction of speciation equilibrium

Matveev et al. (1997) reported experimental measurements of the equilibrium data of C–O–H speciation reactions at 1273 K and 2.4 GPa. Since these data were not used for the parameterization of the model, they provide a strict test of the model. The deviations of different models from the experimental data in terms of the two major species, H_2O and CH_4, are summarized in Fig. 2. It can be seen of all models considered here reproduce the experimental data well, but our model also reproduce the maximum H_2O contents of 94.91 mol%, which falls in the experimental range of 95 ± 1 mol%. The other models (Connolly and Cesare, 1993; Huizenga, 2005) predict lower H_2O contents than observation. The deviations increase to more than 10% when the H_2O maximum is approached. For CH_4, all other models predict higher concentrations than observed with a maximum deviation of ~4 mol% of CH_4. The higher predicted concentrations of CH_4 in other models partly results because they do no consider C_2H_6 in their calculations (Jakobsson and Oskarsson, 1988, 1990).

Fig. 3 shows the remarkable agreement of our model with the experimental data (Matveev et al., 1997) for different species. Although there is no experimental data at other temperatures and pressures available for the validation of the model, we believe this model should be valid in the TP range of 673–2573 K, 1–10,000 MPa, since the equation of state we developed in this study and the strict theoretical calculation of standard chemical potential can be accurately coved in this TP range.

4.3. Model prediction of fluid-graphite/diamond equilibrium

The isobaric–isothermal phase diagram (Fig. 4) provides the basic information on fluid-graphite/diamond equilib-

Table 8
Comparison of $RT \ln f_{CO_2}$ calculated from our equation of state with experimental data.

T (K)	P (MPa)	Thermodynamics data[a]	Exp[b]	Δ	This study	Δ
$MgCO_3 \rightarrow MgO + CO_2$						
1298	500	108.7	107.3	−1.3	106.5	−2.2
1278	700	109.2	115.3	6.1	114.7	5.6
1373	1000	128.4	135.2	6.8	135.1	6.7
1600	1630	172.1	177.1	4.9	178.1	6.0
1700	1920	191.3	195.6	4.3	197.1	5.9
1800	2200	210.0	213.7	3.7	215.6	5.6
$MgCO_3 + SiO_2 \rightarrow MgSiO_3 + CO_2$						
1400	3550	217.0	210.6	−6.4	221.2	4.2
1500	4380	246.6	240.4	−6.2	253.9	7.3
$MgCO_3 + TiO_2 \rightarrow MgTiO_3 + CO_2$						
1200	1240	132.1	129.4	−2.6	130.5	−1.6
1300	1670	154.5	151.8	−2.8	154.2	−0.4
1400	2100	176.8	173.5	−3.3	177.3	0.4
1500	2530	199.0	195.0	−4.1	200.0	1.0
1600	2960	221.1	216.3	−4.7	222.5	1.4
1700	3380	242.9	237.5	−5.4	244.5	1.6
$CaCO_3 \rightarrow CaO + CO_2$						
1200	760	111.9	111.7	−0.1	111.4	−0.5
1300	1060	132.9	131.5	−1.4	131.7	−1.2
1400	1360	153.9	150.5	−3.4	151.4	−2.4
1500	1660	174.8	169.2	−5.6	170.8	−4.0
1600	1950	195.5	187.4	−8.1	189.6	−5.9
1700	2240	216.4	205.6	−10.8	208.3	−8.1

[a] Experimental phase equilibrium data for decarbonization reactions, thermodynamics data from Saxena and Fei (1987) and references therein.
[b] Data from Frost and Wood (1997a).

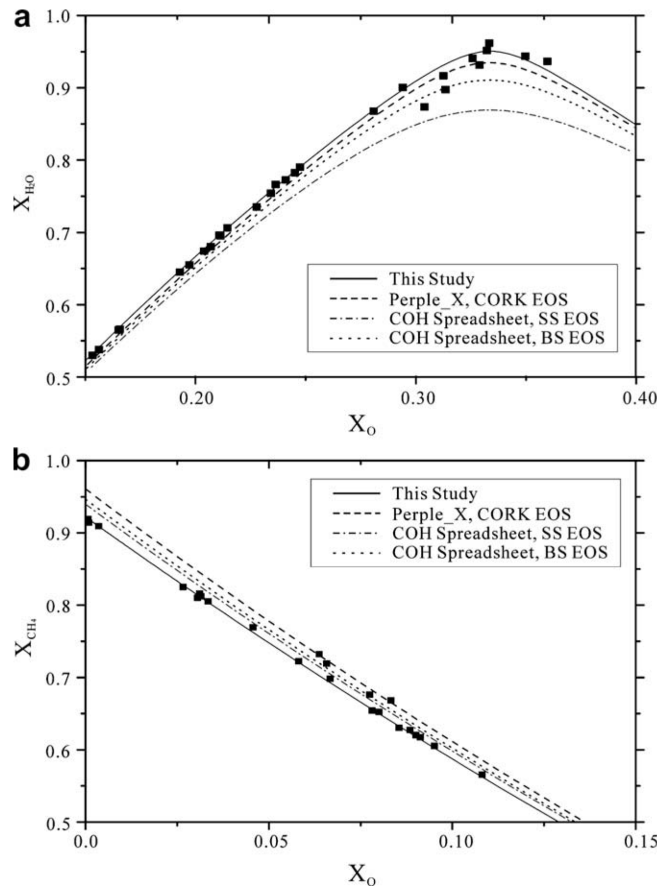

Fig. 2. Comparison of previous models and the model of this study with the experimental results (denoted by solid squares) from Matveev et al. (1997). (a) H_2O contents as a function of X_O and (b) CH_4 content as a function of X_O at 1273 K, 2.4 GPa. The label Perple_X, CORK is calculated from the COHSRK program in Perple_X collection (www.perplex.ethz.ch) with suggested CORK EOS (Connolly and Cesare, 1993; Connolly, 1995). The label COH-spreadsheet SS and BS represent calculated results after the model of Huizenga (2001, 2005) with calculated fugacity coefficients from SS EOS (Shi and Saxena, 1992) and BS EOS (Belonoshko and Saxena, 1992).

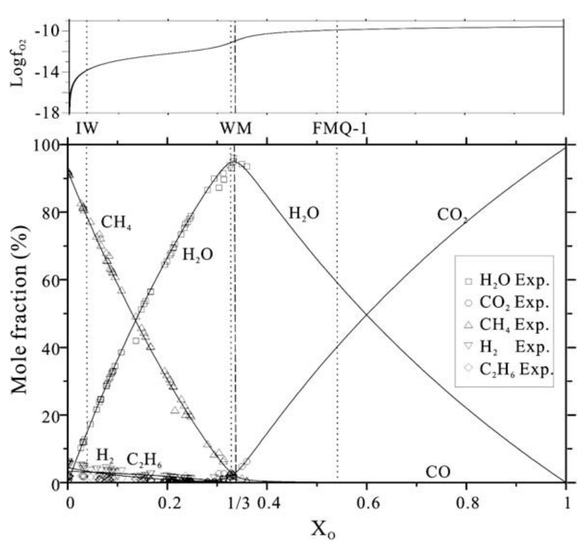

Fig. 3. The predicted composition of the carbon-saturated C–O–H fluid system at 1273 K, 2.4 GPa from this model as compared with experimental data. The solid curve represents the prediction of this model and the symbols stand for experimental data taken from Matveev et al. (1997). The vertical lines represent the corresponding oxygen fugacity.

rium and compositions of the C–O–H system. The carbon-saturation curves divide the phase diagram into two regions: the upper consists of solid graphite/diamond phase coexisting with fluids and the lower region is a fluid phase. In the two phase region, the compositions of coexisting fluid are given by the point of intersection of this boundary with a line through both the bulk composition and the C corner. At $X_O = 1/3$, the coexisting fluid meets the water maximum and carbon minimum; on either side of $X_O = 1/3$, the carbon content in the fluids will increase. The three curves on the figure indicate that decreasing temperature or increasing pressure will shift the carbon-saturated surface away from the C corner, suggesting the precipitation of graphite. For example, a C–O–H fluid at point A, which is saturated with graphite at 1273 K and 2.4 GPa will precipitate graphite when temperature decreases to 1073 K, but it will become unsaturated when pressure drops to 2.0 GPa. The major reaction involved here is the heterogeneous reaction between different valence states of the carbon:

$$CO_2 + CH_4 \rightarrow 2C + H_2O \tag{27}$$

With the progress of this reaction, the ratio X_{CH_4}/X_{CO_2} shifts towards 0 or 1 depending on the initial X_O. If the ini-

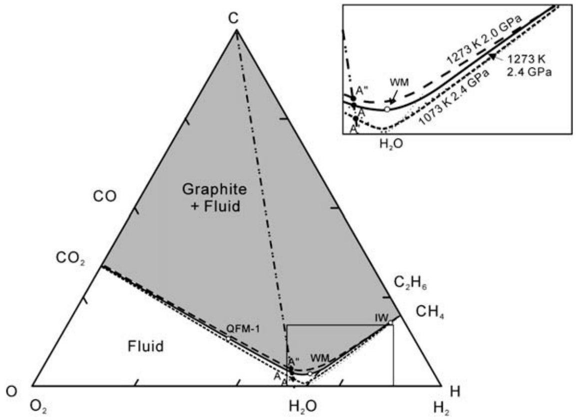

Fig. 4. Isobaric–isothermal phase diagram for the C–O–H system at 1273 K, 2.4 GPa (solid curve), 1273 K, 2.0 GPa (long dash curve) and 1073 K, 2.4 GPa (short dash curve). The dash-dot tie line which starts from the C corner represents the fluid composition with the same X_O. The open circles show the corresponding oxygen fugacity on the carbon-saturated surface to the well-known oxygen fugacity buffer IW (iron–wustite), WM (wustite–magnetite) and FMQ (fayalite–magnetite–quartz). The solid circles located on three different carbon-saturated surfaces are discussed in the text.

tial $X_O > 1/3$, $X_{CH_4} < X_{CO_2}$ like point A, the final composition in lower temperature will be much CO_2 richer; if $X_O < 1/3$, the fluid will become CH_4 dominated. It is worth to note that, as pointed out by Ziegenbein and Johannes (1980), though the reaction in Eq. (27) is thermodynamically sound, the high activation energy requirement of this reaction allow the existence of metastable CO_2 and CH_4 mixture fluid inclusion observed by Van den Kerkhof et al. (1991).

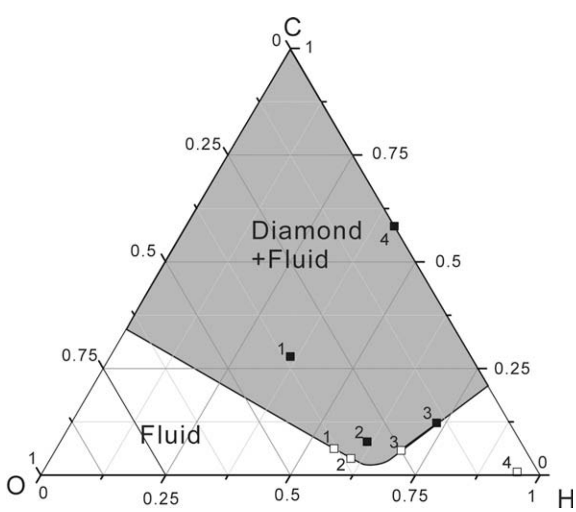

Fig. 5. Diamond crystallization in C–O–H fluid system: experimental *vs.* calculated at 1693.15 K and 5.7 GPa. The solid curve represents the calculated carbon saturated line. The solid and open squares represent the initial and final composition of the experimental data (Sokol et al., 2004), respectively. The numbers marked near these points are used to indentify certain experiment procedure.

The experiments on diamond crystallization from C–O–H fluids (Sokol et al., 2001, 2004) gives more detailed picture on graphite/diamond-fluid phase relationship. Fig. 5 shows the projections of the experimental data (Sokol et al., 2004) measured at 1693.15 K and 5.7 GPa on our calculated phase diagram. Although the experimental capsules cannot seal the system well, as shown by the variation of the H/O ratio, the final diamond-fluid equilibrium points (labels 1 and 2) are just located on the carbon-saturated surface predicted by our model. Point 3 is also located on the diamond saturated surface, but no diamond formation is reported. One possible explanation is that the initial composition is also on the carbon-saturated surface, and the whole system does not vary much from equilibrium and the detection of precipitation is difficult.

5. PREDICTION OF FLUID COMPOSITION IN THE EARTH'S DEEP INTERIOR

Thermodynamic model offer a competitive method for studying fluid compositions in the Earth's deep interior given the difficulty of sampling fluid compositions even only a few kilometers below the surface. Fig. 3 demonstrates the general trend in fluid composition with varying oxygen fugacity under upper mantle P–T condition. For reducing conditions, (e.g., iron–wustite equilibrium (IW)), the fluid composition calculated from our model is dominated by CH_4 (~80 mol%) and H_2O (~14 mol%). We also notice that C_2H_6, and possibly other heavier alkanes, have significant concentrations in this reduced fluid (~4 mol%) and are similar in abundance to H_2 at the same condition. This is consistent with the experimental results of Kenney et al. (2002) at pressures above 3 GPa (~100 km), where the H–C system must evolve ethane and other heavier hydrocarbon compounds. With increasing oxygen fugacity, the calculated results suggest that the mole percent of reductive species CH_4, C_2H_6, H_2 quickly decrease and the system becomes H_2O dominated near the wustite–magnetite equilibrium (WM). As the system approaches fayalite–magnetite–quartz equilibrium (FMQ), the oxidative species CO_2 and CO dominate.

From the validation above, we can reasonably assume that our model can predict C–O–H fluid compositions from lower crust to upper mantle as long as the temperature, pressure and oxygen fugacity are given. The geotherm of the Earth's interior (e.g., T and P) has been defined by mineral phase transitions (Xu et al., 1999; Da Silva et al., 2000; Ichiki et al., 2006; Van der Hilst et al., 2007) or estimated from measurements of heat flow (Pollack and Chapman, 1977; Pollack et al., 1993). However, the oxygen fugacity still needs to be defined.

Over last 20 years, considerable efforts have produced a large amount of data on the oxygen fugacity recorded by mantle rocks or derivative melts and fluids originated from the Earth's deep interior. Although general agreement on the oxidation state offer mantle has not been reached, a relatively consistent redox profiles in cratonic mantle is emerging from the study of mantle xenoliths (Woodland and Koch, 2003; McCammon and Kopylova, 2004; Simakov,

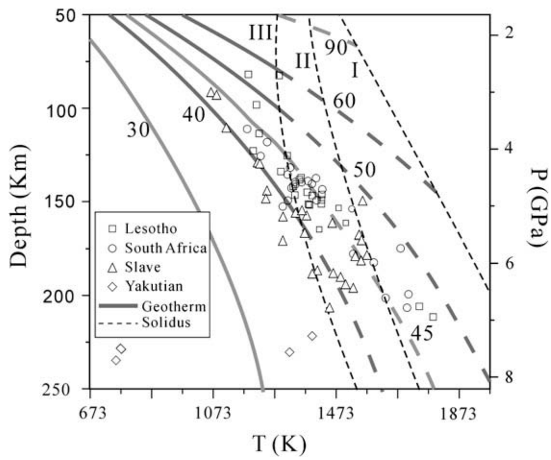

Fig. 6. Thermobarometric data calculated from paragenesis minerals in the xenoliths beneath cratons. The thick solid lines represent the conductive geotherm family for continental terrains (Pollack and Chapman, 1977) where the heat transfer is mainly in the mode of conduction. The number on each geotherm indicates the corresponding surface heat flow (mW/m^2). Dash lines I, II and III show the generalized solidus curves for peridotite in volatile free, mixed volatile and hydrous environments, respectively. Data of Kaapvaal craton are from Woodland and Koch(2003), SLAVE craton from McCammon and Kopylova (2004) and data of Yakutian craton from Simakov (1998). Depth of formation is transformed from multiplying the pressure by 33 Km/1 GPa.

2006). Recently determined redox profile recovered by mantle xenoliths from the Kaapvaal craton (Woodland and Koch, 2003) and Slave craton in northern Canada (McCammon and Kopylova, 2004) using spinel-orthopyroxene-olivine and garnet-orthopyroxene-olivine oxybarometry showed a systematic decrease in fO_2 with depth in the upper cratonic mantle. This supports the earlier predictions of a reduced upper mantle within the garnet peridotite faces (Wood, 1990; Ballhaus and Frost, 1994). Projection of these data onto Fig. 6 shows that the T–P geotherm in this region is generally located in the region between continental conductive surface heat flow 40 and 50 mW/m^2. So we adopt a surface heat flow 45 mW/m^2 model to estimate the T and P (Pollack and Chapman, 1977).

Based on the temperature and pressure and the redox profile, the composition of the fluids as a function of depth and fO_2 are calculated from our model as shown in Fig. 7. These results suggest that most of the mantle redox data points are scattered around the curve of $X_O = 1/3$. The model assumes carbon oversaturation to reduce the degrees of freedom. Most estimates for the bulk carbon content of the mantle are from direct measurements on mantle derived xenoliths (Deines, 2002), volcanic gas (Gerlach et al., 2002) or by analogy with chondrite (Marty and Jambon, 1987) and vary from 2 to 1000+. The experimentally determined carbon solubility in mantle minerals varies in the range of 0.03–15 ppm by weight (Shcheka et al., 2006). The difference here shows that most of carbon in the mantle must be stored in a separate carbon-rich phase. Thus we have calculated the composition of C–O–H fluid in the upper mantle as carbon oversaturated first and then discuss the differences where carbon undersaturated is necessary.

Fig. 7(a) and (b) show that the major C-bearing species in the fluid system changes from CH_4 and C_2H_6 (~20% and ~5% at 220 km depth) to CO_2 (30% at 80 km depth) with the decrease of depth. This is supported by the observation that fluid inclusions in spinel peridotite are mainly CO_2 (Pasteris, 1987) at depths <100 km and that CH_4-rich fluid inclusions are reported in ophiolitic dunite (Liu and Fei, 2006) formed at the depth ~200 km. The ~140–175 km depth marks the transition region where the fluid switches from dominantly H_2O–CH_4 to H_2O–CO_2 dominated. Taylor and Green (1988) suggest that the oxidation of CH_4 in the system will significantly lower the peridotite solidus and induce partial melting. The inferred change may partially support the "redox-melting" hypothesis from Griffin et al. (2003) that the depleted subcontinental lithospheric mantle in this region lies at ~160–175 km.

Under the environment of lower oxygen fugacity indicated by points below ~140–175 km, CH_4 and C_2H_6 are the most stable species in the carbon oversaturated C–O–H system. For instance, CH_4 abundance is >50% and C_2H_6 is >15% as observed in the two Yakutian inclusions in diamonds (Simakov, 1998). The calculated results also support the abiogenic generation of methane in the Earth's mantle by carbonate reduction from FeO, $CaCO_3$-calcite and water, which is consistent with the experimental results of Scott et al. (2004).

As indicated in Fig. 7(c) and (d), H_2O is the principal species in the coexisting fluid system for all three calculated fO_2-depth data sets recorded by mantle xenoliths (label South Africa and Lesotho for the Kaapvaal craton and label Slave for the Slave craton) and H_2O accounts for >50% of the fluid our the range of 80 and 220 km. The ratio of mole fraction of H_2O and CO_2 varies between 1 and 10,000 in data range. The trend of X_{H_2O} reverses at the water maximum line, $X_O = 1/3$, where the fluid system is nearly pure H_2O with $X_{H_2O} > 99\%$. At greater depth (~150–220 km), X_{H_2O} decreases with increasing depth and it reaches ~70% at 220 km, which corresponds to the lowest oxygen fugacity between FMQ-4 and FMQ-5 recorded by spinel peridotite. The X_{H_2O} may be even higher if carbon activity is lower than unity.

To investigate fluid compositions along different geothermal gradient, we calculated the composition of carbon oversaturated COH fluid system with $X_O = 1/3$ under different T and P conditions as shown in Fig. 8. The bottom left corner corresponds to region with lower geothermal gradient, such as Kaapvaal craton and Slave craton mentioned above. In this region, the equilibrium fluid composition is mainly H_2O and variations are not sensitive to the modeled surface heat flow. The upper part represents the region with much higher geothermal gradient, such as the Mesozoic and Cenozoic geotherm in eastern China (Xu, 2001; Zheng et al., 2001). Though the mole percent of H_2O accounts for more than 85% (assuming 90 mW/m^2 surface heat flow), the contribution of other species, such as CO_2 and CH_4, need to be taken into consideration.

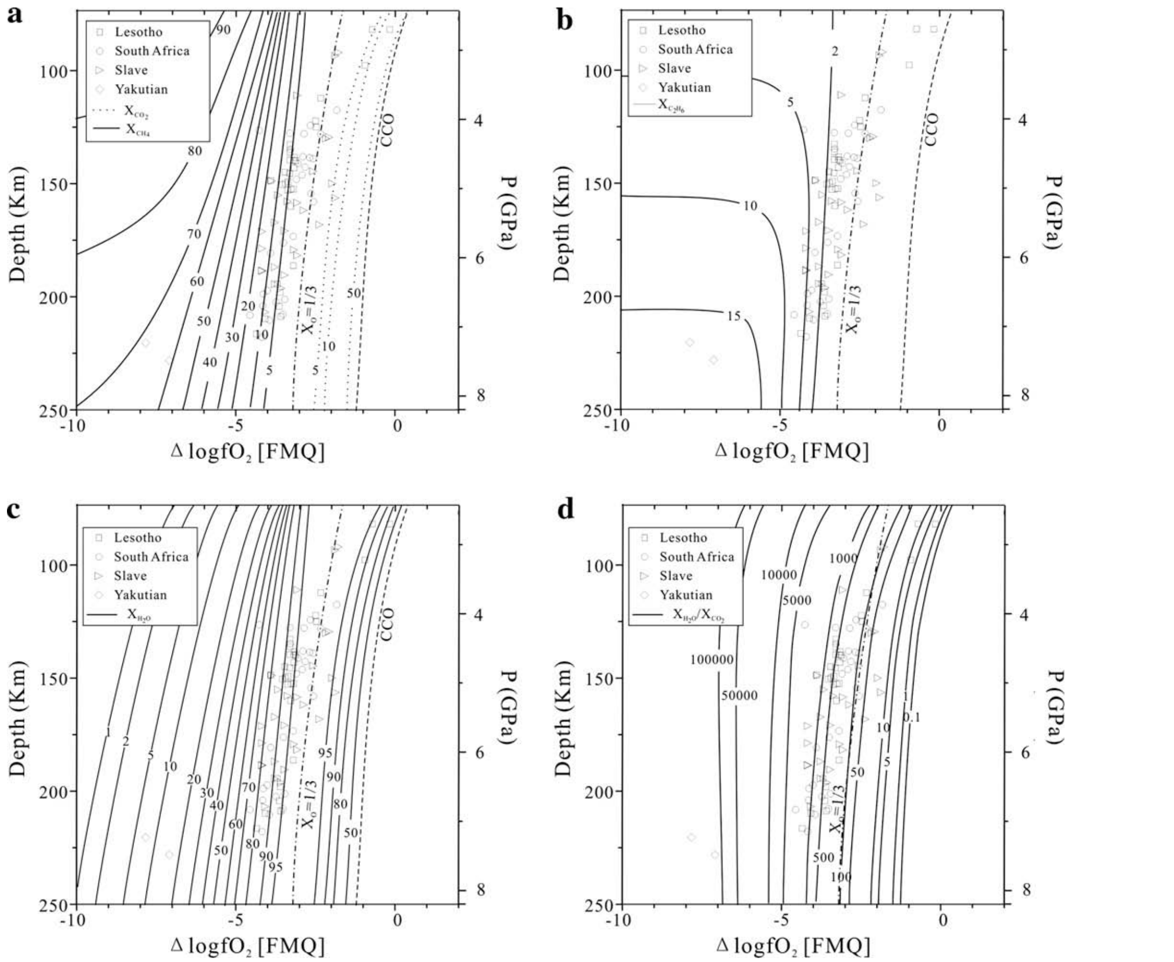

Fig. 7. Prediction of fluid compositions beneath cratons: (a) X_{CH_4} (solid lines) and X_{CO_2} (dot lines); (b) $X_{C_2H_6}$ (solid lines); (c) X_{H_2O} (solid lines); (d) (solid lines). The compositions are calculated following the conductive geotherm corresponding to the surface heat flow 45 mW/m^2 as indicated in Fig. 6. The value of each isopleth of composition is marked nearby. The data points represent the redox profile of Kaapvaal craton (open square, Woodland and Koch (2003)) and Slave craton (open triangles, McCammon and Kopylova (2004)). Paragenesis minerals oxygen barometer measured in inclusions in diamonds of Yakutian craton (open diamond, Simakov (1998)) is also showed.

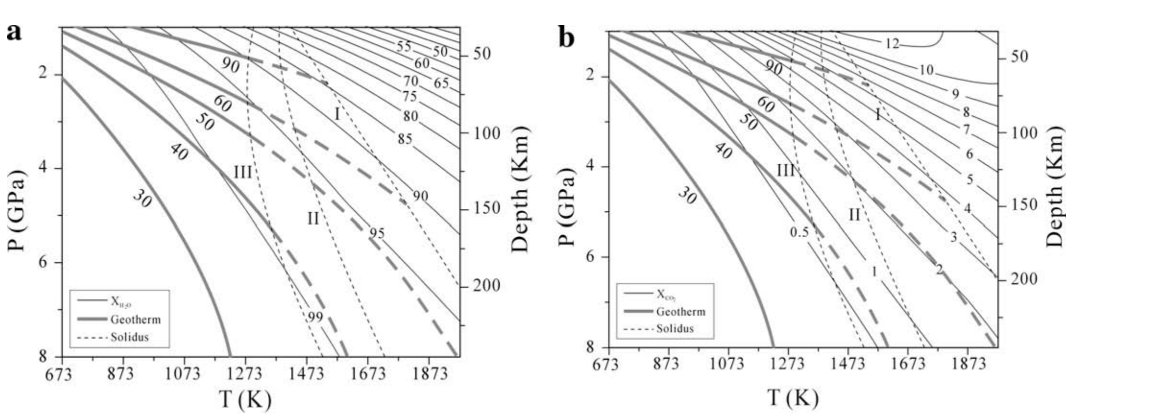

Fig. 8. Variation in equilibrium composition of C–O–H ($X_O = 1/3$) fluid system: (a) X_{H_2O}; (b) X_{CO_2} as a function of T and P. The meaning of the thick lines and dash lines is described in the caption of Fig. 6. The thin lines marked with number are the isopleths in mole percent of H_2O or CO_2.

6. CONCLUSION

Based on strong EOS, statistical mechanics calculation and non-stoichiometric global free-energy minimization, a model is developed to predict the compositions (H_2O, CO_2, CH_4, H_2, CO, O_2 and C_2H_6) of the C–O–H fluid system under high temperatures and pressures of the Earth's upper mantle. Although not fitted from speciation experimental data of C–O–H speciation, the model accurately reproduces all of them, demonstrating that the model should extrapolate beyond the experimental temperature–pressure range.

As calculated from this model, H_2O is the dominated fluid species in the wide *TP* range of the cratonic mantle (~80–220 km depth). In the deeper part, the fluid mainly composed of the mixture of H_2O–CH_4–H_2–C_2H_6. It is very possible to generate methane and ethane under mantle conditions. When fluid ascends across the boundary between lithosphere and asthenosphere, the reduced species may be oxidized and the fluid is mainly composed of H_2O–CO_2–CO.

ACKNOWLEDGMENTS

This work is supported by Zhenhao Duan's "Major development Funds" (code #: kzcx2-yw- 124) by Chinese Academy of Sciences, the "Key Project Funds" (No. 40537032) by National Science Foundation of China and Wenxun Hu's 973 funds Company Supported by the NKBRDPC (Grant No. 2005CB422103) and his funds (40673040) supported by NSFC, and the 973 Project Funds (#2006CB-705800) awarded by the Ministry of Science and Technology of China. We thank Dr. Kelly Russell and two anonymous reviewers for their valuable comments and constructive suggestions.

REFERENCES

Ballhaus C. and Frost B. R. (1994) The generation of oxidized CO_2-bearing basaltic melts from reduced CH_4-bearing upper mantle sources. *Geochim. Cosmochim. Acta* **58**, 4931–4940.

Belonoshko A. B. and Saxena S. K. (1992) A unified equation of state for fluids of C–H–O–N–S–Ar composition and their mixtures up to very high-temperatures and pressures. *Geochim. Cosmochim. Acta* **56**, 3611–3626.

Botchamikov R. E., Behrens H. and Holtz F. (2006) Solubility and speciation of C–O–H fluids in andesitic melt at $T = 1100$–1300 °C and $P = 200$ and 500 MPa. *Chem. Geol.* **229**, 125–143.

Bottinga Y. and Richet P. (1981) High pressure and temperature equation of state and calculation of the thermodynamic properties. *Am. J. Sci.* **281**, 620–659.

Brodholt J. P. and Wood B. J. (1994) Measurements of the PVT properties of water to 25 kbars and 1600 °C from synthetic fluid inclusions in corundum. *Geochim. Cosmochim. Acta* **58**, 2143–2148.

Bruce Watson E. and Brenan J. M. (1987) Fluids in the lithosphere. 1. Experimentally-determined wetting characteristics of CO_2–H_2O fluids and their implications for fluid transport, host-rock physical properties, and fluid inclusion formation. *Earth. Planet. Sci. Lett.* **85**, 497–515.

Churakov S. V. and Gottschalk M. (2003a) Perturbation theory based equation of state for polar molecular fluids. I. Pure fluids. *Geochim. Cosmochim. Acta* **67**, 2397–2414.

Churakov S. V. and Gottschalk M. (2003b) Perturbation theory based equation of state for polar molecular fluids. II. Fluid mixtures. *Geochim. Cosmochim. Acta* **67**, 2415–2425.

Connolly J. A. D. (1995) Phase-diagram methods for graphitic rocks and application to the system C–O–H–FeO–TiO_2–SiO_2. *Contrib. Mineral. Petrol.* **119**, 94–116.

Connolly J. A. D. and Cesare B. (1993) C–O–H–S fluid composition and oxygen fugacity in graphite metapelites. *J. Metamorph. Geol.* **11**, 379–388.

Da Silva C. R. S., Wentzcovitch R. M., Patel A., Price G. D. and Karato S. I. (2000) The composition and geotherm of the lower mantle: constraints from the elasticity of silicate perovskite. *Phys. Earth. Planet. Inter.* **118**, 103–109.

Deines P. (2002) The carbon isotope geochemistry of mantle xenoliths. *Earth Sci. Rev.* **58**, 247–278.

Duan Z. and Zhang Z. (2006) Equation of state of the H_2O, CO_2, and H_2O–CO_2 systems up to 10 GPa and 2573.15 K: Molecular dynamics simulations with ab initio potential surface. *Geochim. Cosmochim. Acta* **70**, 2311–2324.

Duan Z. H., Moller N. and Weare J. H. (1992) Molecular-dynamics simulation of PVT properties of geological fluids and a general equation of state of nonpolar and warkly polar gases up to 2000 K and 20000 bar. *Geochim. Cosmochim. Acta* **56**, 3839–3845.

Duan Z. H., Moller N. and Weare J. H. (1996) A general equation of state for supercritical fluid mixtures and molecular dynamics simulation of mixture PVTX properties. *Geochim. Cosmochim. Acta* **60**, 1209–1216.

French B. M. (1966) Some geological implications of equilibrium between graphite and a C–H–O gas phase at high temperatures and pressures. *Rev. Geophys.* **4**, 223–254.

Frezzotti M. L., Di Vincenzo G., Ghezzo C. and Burke E. A. J. (1990) Evidence of magmatic CO_2-rich fluids in peraluminous graphite-bearing leucogranites from Deep Freeze Range. *Contrib. Mineral. Petrol.* **117**, 111–123.

Fried L. E. and Howard W. M. (2000) Explicit Gibbs free energy equation of state applied to the carbon phase diagram. *Phys. Rev. B Condens. Matter* **61**, 8734–8743.

Frost D. J. and Wood B. J. (1997a) Experimental measurements of the fugacity of CO_2, and graphite/diamond stability from 35 to 77 kbar at 925 to 1650 °C. *Geochim. Cosmochim. Acta* **61**, 1565–1574.

Frost D. J. and Wood B. J. (1997b) Experimental measurements of the properties of H_2O–CO_2 mixtures at high pressures and temperatures. *Geochim. Cosmochim. Acta* **61**, 3301–3309.

Gerlach T. M., McGee K. A., Elias T., Sutton A. J., and Doukas M. P. (2002) Carbon dioxide emission rate of Kilauea Volcano: implications for primary magma and the summit reservoir. *J. Geophys. Res.* **107**, 2189.

Gerya T. V. and Yuen D. A. (2003) Rayleigh-Taylor instabilities from hydration and melting propel 'cold plumes' at subduction zones. *Earth. Planet. Sci. Lett.* **212**, 47–62.

Griffin W. L., O'Reilly S. Y., Natapove L. M. and Ryan C. G. (2003) The evolution of lithospheric mantle beneath the Kalahari craton and its margins. *Lithos* **71**, 215–241.

Gurvich L. V., Iorish V. S., Yungman V. S. and Dorofeeva O. V. (2007) Thermodynamic properties as a function of temperature. In *CRC Handbook of Chemistry and Physics, Internet Version 2007* (ed. D. R. Lide), 87th ed. Taylor and Francis, Boca Raton, FL.

Holland T. and Powell R. (1991) A Compensated-Redlich–Kwong (CORK) equation for volumes and fugacities of CO_2 and H_2O in the range 1 bar to 50 kbar and 100–1600 °C. *Contrib. Mineral. Petrol.* **109**, 265–273.

Holland T. J. B. and Powell R. (1998) An internally consistent thermodynamic data set for phases of petrological interest. *J. Metamorph. Geol.* **16**, 309–343.

Holloway J. R. (1977) Fugacity and activity of molecular species in supercritical fluids. In *Thermodynamics in Geology* (ed. D. Fraser). Reidel, Boston.

Holloway J. R. (1981) Compositions and volumes of supercritical fluids. In *Fluid Inclusions: Application to Petrology* (eds. L. S. Hollister and M. L. Crawford). Mineralogical Society of Canada, London.

Huber K. and Herzberg G. (1979) *Molecular Spectra and Molecular Structure IV Constants of Diatomic Molecules*. Van Rostrand-Reinhold, New York.

Huizenga J. M. (2001) Thermodynamic modeling of C–O–H fluids. *Lithos* **55**, 101–114.

Huizenga J. M. (2005) COH, an Excel spreadsheet for composition calculations in the C–O–H fluid system. *Comput. Geol.* **31**, 797–800.

Huizenga J. M. and Touret J. L. R. (1999) Fluid inclusions in shear zones: the case of the Umwindsi shear zone in the Harare–Shamva–Bindura greenstone belt, NE Zimbabwe. *Eur. J. Mineral.* **11**, 1079–1090.

Ichiki M., Baba K., Obayashi M. and Utada H. (2006) Water content and geotherm in the upper mantle above the stagnant slab: interpretation of electrical conductivity and seismic P-wave velocity models. *Phys. Earth. Planet. Inter.* **155**, 1–15.

Jacobs G. K. and Kerrick D. M. (1981) Methane: an equation of state with application to the ternary system H_2O–CO_2–CH_4. *Geochim. Cosmochim. Acta* **45**, 607–614.

Jakobsson S. and Oskarsson N. (1988) The system C–O–H at low fO_2, high P and T. *EOS* **69**, 515.

Jakobsson S. and Oskarsson N. (1990) Experimental determination of fluid compositions in the system C–O–H at high P and T and low fO_2. *Geochim. Cosmochim. Acta* **54**, 355–362.

Johnson J. W., Oelkers E. H. and Helgeson H. C. (1992) SUPCRT92—a software package for calculation the standard molar thermodynamic properties of minerals, gases, aqueous species, and reaction from 1 bar to 5000 bar and 0 °C to 1000 °C. *Comput. Geol.* **18**, 899–947.

Kenney J. F., Kutcherov V. A., Bendeliani N. A. and Alekseev V. A. (2002) The evolution of multicomponent systems at high pressures. VI. The thermodynamic stability of the hydrogen–carbon system: the genesis of hydrocarbons and the origin of petroleum. *Proc. Natl. Acad. Sci. USA* **99**, 10976–10981.

Kerrick D. M. and Jacobs G. K. (1981) A modified Redlich–Kwong equation for H_2O, CO_2 and H_2O–CO_2 mixtures at elevated temperatures and pressures. *Am. J. Sci.* **281**, 735–767.

Kress V. C., Ghiorso M. S. and Lastuka C. (2004) Microsoft Excel spreadsheet-based program for calculating equilibrium gas speciation in the C–O–H–S–Cl–F system. *Comput. Geol.* **30**, 211–214.

Larrieu T. L. and Ayers J. C. (1997) Measurements of the pressure–volume–temperature properties of fluids to 20 kbar and 1000 °C: a new approach demonstrated on H_2O. *Geochim. Cosmochim. Acta* **61**, 3121–3134.

Larsen R. B. (1993) Geofluid—a FORTRAN-77 program to compute chemical-properties of gas species in C–O–H fluids. *Comput. Geol.* **19**, 1295–1320.

Liu W. and Fei P. X. (2006) Methane-rich fluid inclusions from ophiolitic dunite and post-collisional mafic-ultramafic intrusion: The mantle dynamics underneath the Palaeo-Asian Ocean through to the post-collisional period. *Earth. Planet. Sci. Lett.* **242**, 286–301.

Liu Y. (2005) Generation and evolution of basaltic magmas: some basic concepts and a new view on the origin of Mesozoic–Cenozoic basaltic volcanism in eastern China. *Geol. J. China Univ.* **11**, 9–46.

Marty B. and Jambon A. (1987) C^3/He in volatile fluxes from the solid Earth: implications for carbon geodynamics. *Earth. Planet. Sci. Lett.* **83**, 16–26.

Matveev S., Ballhaus C., Fricke K., Truckenbrodt J. and Ziegenbein D. (1997) Volatiles in the Earth's mantle. 1. Synthesis of CHO fluids at 1273 K and 2.4 GPa. *Geochim. Cosmochim. Acta* **61**, 3081–3088.

McCammon C. and Kopylova M. G. (2004) A redox profile of the Slave mantle and oxygen fugacity control in the cratonic mantle. *Contrib. Mineral. Petrol.* **148**, 55–68.

McCollom T. M. and Shock E. L. (1998) Fluid–rock interactions in the lower oceanic crust: thermodynamic models of hydrothermal alteration. *J. Geophys. Res.* **103**, 547–575.

Ohmoto H. and Kerrick D. (1977) Devolatilization equilibria in graphitic systems. *Am. J. Sci.* **277**, 1013–1044.

Pasteris J. D. (1987) Fluid inclusions in mantle xenoliths. In *Mantle Xenoliths* (ed. P. H. Nixon). Wiley, New York.

Pollack H., Hurter S. and Johnson J. (1993) Heat flow from the earth's interior—analysis of the global data set. *Rev. Geophys.* **31**, 267–280.

Pollack H. N. and Chapman D. S. (1977) On the regional variation of heat flow, geotherms, and lithospheric thickness. *Tectonophysics* **38**, 279–296.

Rupke L. H., Morgan J. P., Hort M. and Connolly J. A. D. (2004) Serpentine and the subduction zone water cycle. *Earth. Planet. Sci. Lett.* **1-2**, 17–34.

Saxena S. K. and Fei Y. (1987) High pressure and high temperature fluid fugacities. *Geochim. Cosmochim. Acta* **51**, 783–791.

Scott H. P., Hemley R. J., Mao H. K., Herschbach D. R., Fried L. E., Howard W. M. and Bastea S. (2004) Generation of methane in the Earth's mantle: in situ high pressure–temperature measurements of carbonate reduction. *Proc. Natl. Acad. Sci. USA* **101**, 14023–14026.

Shcheka S. S., Wiedenbeck M., Frost D. J. and Keppler H. (2006) Carbon solubility in mantle minerals. *Earth. Planet. Sci. Lett.* **245**, 730–742.

Shi P. F. and Saxena S. K. (1992) Thermodynamic modeling of the C–H–O–S fluid system. *Am. Mineral.* **77**, 1038–1049.

Shimanouchi T. (1972) *Tables of Molecular Vibrational Frequencies Consolidated Volume I*. National Bureau of Standards, Washington, DC.

Simakov S. K. (1998) Redox state of Earth's upper mantle peridotites under the ancient cratons and its connection with diamond genesis. *Geochim. Cosmochim. Acta* **62**, 1811–1820.

Simakov S. K. (2006) Redox state of eclogites and peridotites from sub-cratonic upper mantle and a connection with diamond genesis. *Contrib. Mineral. Petrol.* **151**, 282–296.

Smith W. R. and Missen R. W. (1982) *Chemical reaction equilibrium analysis*. Wiley-Interscience Publication, New York.

Sokol A. G., Pal'yanov Y. N., Pal'yanov G. A. and Tomilenko A. A. (2004) Diamond crystallization in fluid and carbonate-fluid systems under mantle PT conditions. 1. Fluid composition. *Geochem. Int.* **42**, 830–838.

Sokol A. G., Pal'yanov Y. N., Pal'yanova G. A., Khokhryakov A. F. and Borzdov Y. M. (2001) Diamond and graphite crystallization from C–O–H fluids under high pressure and high temperature conditions. *Diam. Relat. Mater.* **10**, 2131–2136.

Spandler C., Hermann J., Arculus R. and Mavrogenes J. (2003) Redistribution of trace elements during prograde metamorphism from lawsonite blueschist to eclogite facies; implications for deep subduction-zone processes. *Contrib. Mineral. Petrol.* **146**, 205–222.

Stalder R., Foley S. F., Brey G. P. and Horn I. (1998) Mineral aqueous fluid partitioning of trace elements at 900–1200 °C and 3.0–5.7 GPa: new experimental data for garnet, clinopyroxene, and rutile, and implications for mantle metasomatism. *Geochim. Cosmochim. Acta* **62**, 1781–1801.

Taylor W. R. and Green D. H. (1988) Measurement of reduced peridotite-C–O–H solidus and implications for redox melting of the mantle. *Nature* **332**, 349–352.

Van den Kerkhof A. M., Touret J. L. R., Maijer C. and Jansen J. B. H. (1991) Retrograde methane-dominated fluid inclusions from high-temperature granulites of Rogaland, southwestern Norway. *Geochim. Cosmochim. Acta* **55**, 2533–2544.

Van der Hilst R. D., De Hoop M. V., Wang P., Shim S.-H., Ma P. and Tenorio L. (2007) Seismostratigraphy and thermal structure of Earth's core-mantle boundary region. *Science* **315**, 1813–1817.

Wallace P. J., Benedetto De V., and Robert J. B. (2003) From mantle to atmosphere: magma degassing, explosive eruptions, and volcanic volatile budgets. *Developments in Volcanology*. Elsevier.

Withers A. C., Kohn S. C., Brooker R. A. and Wood B. J. (2000) A new method for determining the P–V–T properties of high-density H_2O using NMR: results at 1.4–4.0 GPa and 700–1100 °C. *Geochim. Cosmochim. Acta* **64**, 1051–1057.

Wood B. J. (1990) An experimental test of the spinel peridotite oxygen barometer. *J. Geophys. Res.* **95**, 15845–15851.

Woodland A. B. and Koch M. (2003) Variation in oxygen fugacity with depth in the upper mantle beneath the Kaapvaal craton, Southern Africa. *Earth. Planet. Sci. Lett.* **214**, 295–310.

Xu Y., Lin C. and Shi L. (1999) The geotherm of the lithosphere beneath Qilin, SE China: a re-appraisal and implications for *P*–*T* estimation of Fe-rich pyroxenites. *Lithos* **47**, 181–193.

Xu Y. G. (2001) Thermo-tectonic destruction of the Archaean lithospheric keel beneath the Sino-Korean craton in China: evidence, timing and mechanism. *Phys. Chem. Earth* **26**, 747–757.

Zhang C., Duan Z. H. and Zhang Z. G. (2007) Molecular dynamics simulation of the CH_4 and CH_4–H_2O systems up to 10 GPa and 2573 K. *Geochim. Cosmochim. Acta* **71**, 2036–2055.

Zhang Z. G. and Duan Z. H. (2005) Prediction of the PVT properties of water over wide range of temperatures and pressures from molecular dynamics simulation. *Phys. Earth. Planet. Inter.* **149**, 335–354.

Zheng J. P., Sun M., Lu F. X., Wang C. Y. and Zhong Z. Q. (2001) Garnet-bearing granulite facies rock xenoliths from late Mesozoic volcaniclastic breccia, Xinyang, Henan Province. *Acta Geol. Sin. Engl. Ed.* **75**, 445–451.

Zheng Y. F., Fu B., Xiao Y. L., Li Y. L. and Gong B. (1999) Hydrogen and oxygen isotope evidence for fluid–rock interactions in the stages of pre- and post-UHP metamorphism in the Dabie Mountains. *Lithos* **46**, 677–693.

Ziegenbein D. and Johannes W. (1980) Graphite in C–O–H fluids: an unsuitable compound to buffer fluid composition at temperature up to 700 °C. *N. Jb. Mineral. Mh.* **7**, 289–305.

Associate editor: J. Kelly Russell